scientific reports

OPEN

Synchronous reluctance motor speed control based on multivariable Super-Twisting

Yinhang Ning✉, Zhihao Huang, Hengxuan Hou, Renjie Li, Wang Sun & Jiahao He

In order to address issues such as high chattering and insufficient anti-disturbance performance in Synchronous Reluctance Motor (SynRM) speed control systems, this paper proposes an Adaptive Multi-variable Super-Twisting Sliding Mode (AM-STSM) control strategy. First, based on the mathematical model in d-q coordinates, the torque generation principle of SynRM is analyzed. Based on this, an AM-STSM speed controller is designed by introducing time-varying gain terms, achieving rapid convergence when far from the sliding surface and effective suppression of chatter when approaching it. Furthermore, an adaptive Luenberger observer (ALDO) is constructed to observe and compensate for lumped disturbances, significantly enhancing system robustness. In "torque realization" mode, a "Maximum Torque Per Amperage control strategy" is adopted to improve stator current utilization. Simulation and experimental results demonstrate that compared to traditional STSM control methods, the proposed ALDO-AM-STSM approach achieves faster convergence during no-load startup (21.21% reduction). Under sudden load and unload conditions, the speed drop (decreased by 82.67%), speed overshoot (decreased by 88.95%), and adjustment time (sudden load: decreased by 47.97%; sudden unload: decreased by 50.36%) are all significantly decreased. Meanwhile, torque and speed fluctuations during steady-state operation are minimized. This control strategy effectively enhances the dynamic performance and anti-disturbance capability of the SynRM speed control system.

Keywords Synchronous reluctance motor, Multivariable Super-Twisting sliding mode control, Disturbance observer, Adaptive term

Synchronous Reluctance Motors (SynRM) are a type of motor that operates using reluctance torque, representing one of the current research hotspots[1]. The rotors of these motors are all iron cores, lacking permanent magnets or excitation windings, offering distinct advantages particularly under high-speed operation, high-temperature, and humid conditions. Additionally, this motor features simple manufacturing processes, low cost, and minimal rotor losses[2,3]. In applications such as electric vehicles and traction machines, SynRM has emerged as a strong competitor to high-efficiency Induction Motors (IM) or partially Permanent Magnet Synchronous Motors (PMSM)[4–6]. In recent years, structural optimizations have significantly improved the electrical performance of SynRM motors, including power factor, efficiency, and torque quality[7]. However, the inherent complexity of these motors, coupled with nonlinear and uncertain parameters and external disturbances, makes their effective control highly challenging[8].

Linear Proportional-Integral (PI) control, due to its simple structure and ease of implementation, is widely used in speed regulation systems. However, when confronted with time-varying system parameters and external disturbances, PI control struggles to meet high-performance control requirements[9]. Consequently, nonlinear control algorithms have emerged. In recent years, driven by rapid advancements in microprocessor chip computing power, nonlinear control algorithms such as Active Disturbance Rejection Control[10], Feedback Linearization[11], Model Predictive Control[12], and Sliding Mode Control[13] have been applied to SynRM speed control. Today, Sliding Mode Control (SMC) stands out among numerous nonlinear control strategies due to its characteristics of low sensitivity to parameter variations, strong anti-disturbance capability, and high tracking accuracy[14]. Among numerous nonlinear control strategies, SMC stands out and is widely applied in AC motor control.

Traditional first-order SMC suffers from significant chattering issues due to its use of discontinuous switching functions[15]. To address this chattering problem, higher-order sliding mode algorithms emerged, among which Super-Twisting Sliding Mode (STSM) gained significant attention. It was shown in[16] that

School of Electrical Engineering, Shanghai Dianji University, Shanghai 201306, China. ✉email: huangzh2097@163.com

among four second-order sliding mode algorithms, Twisting and STSM demonstrated outstanding dynamic performance improvements. Furthermore, STSM control exhibited superior convergence speed and response speed compared to Twisting. In[17], STSM was applied to the control of doubly-fed induction generators to reduce instantaneous power error. However, the convergence speed of traditional STSM strategies remains suboptimal. To further enhance convergence speed and robustness, Ref.[18] incorporates a linear term into STSM, proposing a multivariable STSM control strategy. This approach effectively improves convergence speed and robustness. Yet, due to the difficulty in determining disturbance upper bounds, larger sliding mode control gains must be designed to ensure control performance, which exacerbates chattering phenomena. To improve the response speed and stability of systems using multivariable STSM under different operating conditions, Ref.[19] replaced the sign function with a sigmoid function. However, the use of the sigmoid function slows down the convergence speed to some extent.

To relieve the chattering problem in sliding mode control, another effective approach is to employ disturbance observers[20]. Integrating disturbance observers as feedforward compensation terms in SMC can effectively anticipate and counteract disturbances, thereby enhancing the anti-disturbance capability of the control system[21]. Reference[22] designed quasi-sliding mode observers and nonlinear disturbance observers for load disturbance estimation, noting the superior estimation speed of the quasi-sliding mode observer. Reference[23] combined a novel disturbance observer with STSM technology to reduce sliding-mode control gains, thereby enhancing the control system's disturbance rejection capability. However, the designed observer employed constant gains, making it difficult to achieve a balance between dynamic response and steady-state error. Reference[24] employs a sliding mode disturbance observer with feedforward compensation for multivariable STSM. By incorporating an adaptive term into the multivariable STSM, it further reduces the chattering issues caused by excessively large gain values in the design. Reference[25] similarly combines a multivariable STSM with adaptive terms and a disturbance observer for PMSM speed control. Nevertheless, the observers in both[24] and [25] feature numerous adjustable parameters, increasing parameter tuning complexity and controller development time.

It should be noted that the above literature primarily discusses the application of SMC strategies and disturbance observers in PMSM control. Compared to PMSM control, control research for SynRM is still in its infancy. Regarding SynRM, Ref.[26] experimentally analyzed for the first time the performance of STSM applied to SynRM speed control. Compared to traditional SMC, STSM exhibits superior response performance and reduced chattering under parameter variations and external disturbances. To enhance system robustness and control accuracy, Ref.[27] fully replaces the PI controller with a third-order sliding mode strategy for both speed and dq-axis current control. However, neither Ref.[26] nor Ref.[27] addresses disturbance compensation. Reference[28] employs a generalized STSM algorithm to construct a speed controller and disturbance observer for SynRM speed control. Simulation results demonstrate that this strategy effectively improves the system's disturbance rejection capability. Reference[29] similarly employs a disturbance observer-based feedforward compensation SMC strategy, combining an extended state observer with high-order sliding mode control incorporating adaptive gains. This approach effectively reduces chattering issues and accelerates convergence. However, neither the strategy proposed in[28] nor that in [29] has been validated for practical engineering applications. Reference[30] experimentally investigates the application of adaptive nonsingular terminal sliding mode control and nonlinear disturbance observers in SynRM speed control. Results demonstrate that this strategy effectively enhances system dynamic performance and robustness. However, this control strategy involves numerous adjustable parameters and is relatively complex, placing high demands on both the system's software and hardware.

This paper investigates a dual-loop vector control system (current loop and speed loop) for SynRM. The current loop employs PI control and implements current sharing based on the Maximum Torque Per Ampere (MTPA) control strategy to enhance stator current utilization. The speed loop innovatively adopts a combined approach of a sliding mode control algorithm (STSM) and feedforward compensation. The STSM unit incorporates an adaptive term, forming an adaptive multi-variable STSM (AM-STSM), while the feedforward compensation unit employs an adaptive Luenberger disturbance observer (ALDO) to enhance the system's disturbance rejection capability. Combining ALDO with AM-STSM yields the ALDO-AM-STSM control strategy. Finally, the performance of this speed control system is analyzed through both simulation and experimental methods, validating the feasibility of the proposed approach. The main contributions of this paper can be summarized in the following three aspects:

1) A AM-STSM control scheme has been designed, which automatically adjusts sliding mode gain values based on error states. This effectively accelerates settling time while reducing oscillations near the sliding surface. Stability analysis was performed using Lyapunov functions.This approach effectively accelerates the adjustment time while reducing chattering near the sliding surface. Stability analysis was performed using the Lyapunov function.
2) A ALDO was constructed to implement feedforward compensation for the speed controller. The observer gain matrix, incorporating an adaptive term, accelerates convergence speed and reduces observation fluctuations, thereby enhancing the system's anti-disturbance capability.
3) Using a combined simulation and experimental approach, the characteristics of a speed control system for SynRM based on ALDO-AM-STSM were investigated, with comparative analysis conducted against STSM and AM-STSM.

The structure of this paper is as follows: Sect. SynRM speed controller design first establishes the mathematical model of SynRM, details the design process of the AM-STSM controller and ALDO, constructs a Lyapunov function to analyze the stability conditions of the controller, and concludes with a discussion of the MTPA current control algorithm. Section Simulation verification and analysis simulates and compares the performance of STSM, AM-STSM, and the proposed ALDO-AM-STSM controllers. Section Experimental validation and

(a) SynRM rotor

(b) Rotor model

Fig. 1. Internal structure of SynRM. (**a**) SynRM rotor, (**b**) Rotor model.

$$u_{ABC} = R_s i_{ABC} + \frac{d}{dt}\left(M_{ABC} + L_{ABC}\right) i_{ABC} \tag{1}$$

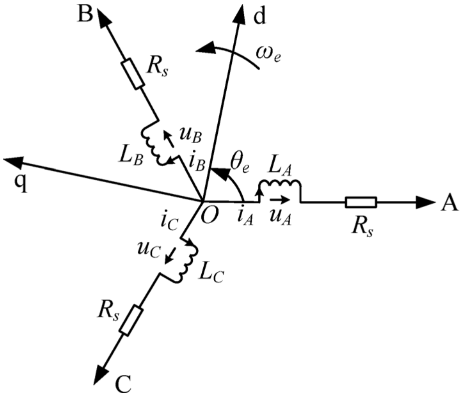

Fig. 2. SynRM A-B-C Coordinate System Equivalent Model.

analysis presents experimental investigations of the proposed control scheme. Section Conclusions gives the conclusions.

SynRM speed controller design

SynRM and its mathematical model

The rotor of SynRM is shown in Fig. 1. It can be seen that the rotor is composed only of an iron core and an air magnetic barrier. The quadrant axis (i.e., the q-axis direction) of this motor primarily comprises the air magnetic gap, which has low magnetic permeability. The direct axis (i.e., the d-axis direction) primarily consists of the iron core material, which has high magnetic permeability. This unique rotor magnetic circuit structure results in unequal d-axis and q-axis inductance parameters L_d and L_q, where $L_d > L_q$. According to the motor's torque generation principle, when $L_d \neq L_q$, reluctance torque can be formed.

The stator windings of the SynRM are identical to those of conventional AC motors. The three-phase windings A-B-C can be equivalently represented as shown in Fig. 2. The electrical angle θ_e is the angle between the d-axis and the axis of phase A, and ω_e is the electrical angular velocity. The voltage equation obtained in the three-phase coordinate system based on Fig. 2 is given by Eq. (1) [31]. In the equation, where u_{ABC}, i_{ABC}, R_s, M_{ABC}, and L_{ABC} represent the voltage, current, resistance, mutual inductance, and self-inductance of the A-B-C three-phase stator winding, respectively.

$$u_{ABC} = R_s i_{ABC} + \frac{d}{dt}\left(M_{ABC} + L_{ABC}\right) i_{ABC} \tag{1}$$

In the analysis of vector control systems for SynRM, the d-q axis rotating coordinate system model is widely adopted. After applying Clark and Park transformations to Eq. (1), the d-q coordinate system mathematical model for SynRM is obtained, as shown in Eq. (2) [32]. Since SynRM lacks a rotor magnetic field excitation source, the voltage equation contains no rotor magnetic flux term. This represents a significant distinction from conventional synchronous motors.

$$\begin{cases} u_d = R_s i_d + L_d \dfrac{di_d}{dt} - \omega_e L_q i_q \\ u_q = R_s i_q + L_q \dfrac{di_q}{dt} + \omega_e L_d i_d \end{cases} \tag{2}$$

In Eq. (2), u_d and u_q represent the stator voltage components in the d-q axes, i_d and i_q denote the stator current components in the d-q axes, R_s is the stator resistance, and ω_e is the electrical angular velocity.

The electromagnetic torque T_e and motion equations of SynRM, as shown in Eq. (3) [33].

$$\begin{cases} \dfrac{d\omega_m}{dt} = \dfrac{T_e}{J} - \dfrac{T_L}{J} - \dfrac{B}{J}\omega_m \\ T_e = \dfrac{3}{2} p_n \left(Ld - Lq\right) i_d i_q \end{cases} \tag{3}$$

In the equation, ω_m is the mechanical angular velocity, T_L is the load torque, B is the friction coefficient, J is the moment of inertia, and p_n is the number of pole pairs.

Improved STSM speed controller design

The control system studied in this paper comprises a speed loop and a current loop. The speed control loop employs an improved SMC algorithm, while the current control loop utilizes an MTPA control algorithm. To discuss the speed loop design, first define the sliding surface $s = e_\omega = \omega_m - \omega_m^*$, where $\omega_m{}^*$ represents the desired mechanical angular velocity. Within the control cycle, $\omega_m{}^*$ can be considered constant, allowing Eq. (3) to be simplified to Eq. (4). Here, $h(t)$ is the lumped disturbance.

$$\begin{cases} \dfrac{ds}{dt} = \dfrac{de_\omega}{dt} = \dfrac{d\left(\omega_m - \omega_m^*\right)}{dt} = \dfrac{T_e^*}{J} + \dfrac{\left(T_e - T_e{}^*\right)}{J} - \dfrac{T_L}{J} - \dfrac{B\omega_m}{J} = \dfrac{T_e^*}{J} + h\left(t\right) \\ h(t) = \dfrac{1}{J}\left(\left(T_e - T_e{}^*\right) - T_L - B\omega_m\right) \end{cases} \tag{4}$$

To further enhance convergence speed and mitigate chattering caused by excessively large SMC gain values, an adaptive multi-variable STSM (AM-STSM) algorithm was developed, as shown in Eq. (5).

$$\begin{cases} \dfrac{ds}{dt} = -k_1 |s|^{\frac{1}{2}} sign(s) - k_2 \varepsilon_1\left(t\right) s + u_1 \\ \dfrac{du_1}{dt} = -k_3 \varepsilon_2\left(t\right) sign(s) - k_4 s \end{cases} \tag{5}$$

In the equation, $k_1 > 0$, $k_2 > 0$, $k_3 > 0$, and $k_4 > 0$ are the gain values to be designed. $\varepsilon_1\left(t\right)$ and $\varepsilon_2\left(t\right)$ are adaptive terms, as shown in Eq. (6).

$$\begin{cases} \varepsilon_1\left(t\right) = \dfrac{1}{\eta_1 + \left(1 + |s|^{-1} - \eta_1\right) e^{-|s|}} \\ \varepsilon_2\left(t\right) = \dfrac{1}{\eta_1 + \left(1 - \eta_1\right) e^{-|s|}} \end{cases} \tag{6}$$

In Eq. (6), $0 < \eta_1 < 1$. When the system trajectory is far from the sliding surface (i.e., $|s|$ is large), both $\varepsilon_1\left(t\right)$ and $\varepsilon_2\left(t\right)$ converge to $\eta_1{}^{-1}$ (greater than 1). As the distance to the sliding surface decreases (i.e., $|s|$ is small), $\varepsilon_1\left(t\right)$ and $\varepsilon_2\left(t\right)$ gradually approaches 0 and 1, respectively.

From Eq. (4), it can be seen that s is influenced by both $T_e{}^*$ and $h(t)$. Therefore, two cases can be considered during design.

(1) When neglecting $h(t)$.

When designing a speed controller, if $h(t)$ is neglected and only $T_e{}^*$ is considered, then based on Eq. (4) and Eq. (5), the AM-STSM speed controller shown in Eq. (7) can be obtained.

$$\begin{cases} T_e{}^* = J\left[-k_1 |e_\omega|^{\frac{1}{2}} sign(e_\omega) - k_2 \varepsilon_1\left(t\right) e_\omega + u_1\right] \\ \dfrac{du_1}{dt} = -k_3 \varepsilon_2\left(t\right) sign(e_\omega) - k_4 e_\omega \end{cases} \tag{7}$$

Considering the characteristics of $\varepsilon_1(t)$ and $\varepsilon_2(t)$, it can be seen that when the system trajectory deviates significantly from the sliding surface, $k_2\varepsilon_1(t)$ and $k_3\varepsilon_2(t)$ increase to $k_2\eta_1{}^{-1}$ and $k_3\eta_1{}^{-1}$, respectively. When approaching the sliding mode surface, the $k_2\varepsilon_1(t)$ and $k_3\varepsilon_2(t)$ terms decrease to 0 and k_3, respectively. It is evident that the AM-STSM automatically adjusts the gain coefficients based on the magnitude of s. This demonstrates that the control scheme not only enhances the system's convergence speed but also suppresses chattering near the stable phase.

During motor startup, excessive rotational speed deviation can cause the integral term to saturate. This leads to severe overshoot in the speed control system and even oscillation. To this end, a saturation limiter module *Sat* with a saturation value of $T_{es}{}^{*}$ is incorporated into the speed control loop, and an anti-windup coefficient ξ is introduced. When the integration term is unsaturated, $\xi=1$; when the integration is saturated (i.e., $|T_e{}^{*}| > |T_{es}^{*}|$), $\xi = -1$, causing the integration term to exit saturation. After incorporating the anti-windup coefficient, the AM-STSM speed controller is expressed as Eq. (8). Based on Eq. (8), the constructed AM-STSM speed controller is shown in Fig. 3.

$$\begin{cases} T_e{}^{*} = J\left[-k_1|e_\omega|^{\frac{1}{2}}sign(e_\omega) - k_2\varepsilon_1(t)\,e_\omega + u_1\right] \\ \dfrac{du_1}{dt} = -k_3\varepsilon_2(t)\,sign(e_\omega) - k_4\xi e_\omega \end{cases} \tag{8}$$

(2) When considering $h(t)$.

To enhance the system's dynamic response, the influence of $h(t)$ is further considered during speed control design. An LDO is employed to obtain disturbance estimates $\hat{h}(t)$ and perform feedforward compensation. To facilitate observer design, the mathematical model of the SynRM speed control system is reformulated into state-space form as shown in Eq. (9). In the equation, the variation of $h(t)$ is relatively slow compared to the sampling period of the speed loop, allowing the derivative of $h(t)$ to be considered equal to zero.

$$\begin{cases} \dfrac{dx}{dt} = ax + bu \\ y = cx \end{cases} \tag{9}$$

In the equation, the state variable $x = \begin{bmatrix} \omega_m & h(t) \end{bmatrix}^{\mathrm{T}}$, the system output $y = \omega_m$, the control input $u = T_e^{*}$, the input matrix $b = \begin{bmatrix} \frac{1}{J} & 0 \end{bmatrix}^{\mathrm{T}}$, the output matrix $c = \begin{bmatrix} 1 & 0 \end{bmatrix}$, and the state transition matrix $a = \begin{bmatrix} 0 & 1 \\ 0 & 0 \end{bmatrix}$.

According to Eq. (9), the designed LDO is given by Eq. (10) [14]. In this equation, $\hat{y}$ and $\hat{x}$ represent the estimated values of y and x, respectively, while $l = \begin{bmatrix} l_1 & l_2 \end{bmatrix}^{\mathrm{T}}$ denotes the gain value of the observer, which is an undetermined parameter.

$$\begin{cases} \dfrac{d\hat{x}}{dt} = a\hat{x} + bu + l\,(y - \hat{y}) \\ y = c\hat{x} \end{cases} \tag{10}$$

To determine the value of l, the error equation for x is further provided as in Eq. (11), where $\tilde{x} = x - \hat{x}$ represents the estimation error of x.

$$\frac{d\tilde{x}}{dt} = a\,(x - \hat{x}) + l\,(y - \hat{y}) = (a + lc)\,\tilde{x} \tag{11}$$

The characteristic equation of Eq. (11) is clearly given by Eq. (12). Here, I denotes the identity matrix and λ represents the eigenvalues.

$$|\lambda I - (a - lc)| = \lambda^2 + \alpha_1\lambda + \alpha_2 = 0 \tag{12}$$

Solving Eq. (12) reveals that selecting $l_1 = 2\alpha_1, l_2 = \alpha_1^2$ and $\alpha_1 > 0$ enables $\lambda < 0$ (i.e., LDO convergence). Clearly, the magnitude of α_1 affects the convergence speed of LDO: a larger α_1 results in faster convergence of the observer. However, an excessively large α_1 leads to significant overshoot and poor steady-state performance.

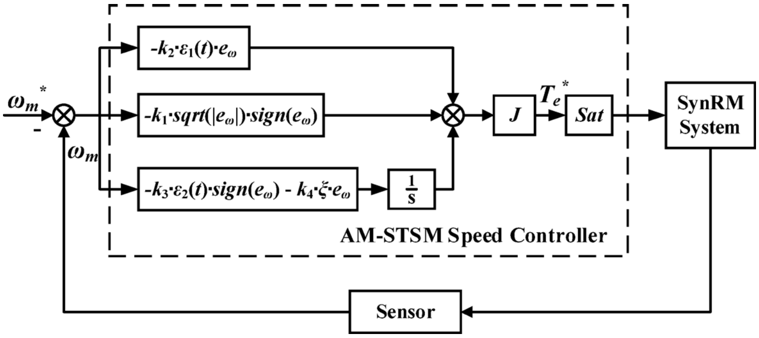

Fig. 3. AM-STSM Speed Controller Block Diagram.

To endow l with adaptive characteristics, $l = \begin{bmatrix} 2\varepsilon_3\left(t\right)\alpha_1 & \left(\varepsilon_3\left(t\right)\alpha_1\right)^2 \end{bmatrix}^{\mathrm{T}}$ is adopted, where $\varepsilon_3\left(t\right)$ is defined as in Eq. (13).

$$\varepsilon_3\left(t\right) = \frac{1}{\eta_2 + k\left(1 - \left(1 + e^{-k|e_\omega|}\right)^{-1}\right)} \tag{13}$$

From the above analysis, it is evident that during operation, the observer requires both the actual rotational speed value ω_m and the estimated rotational speed value $\hat{\omega}_m$. Therefore, combining Eq. (10) and Eq. (13) yields an adaptive LDO (ALDO) as expressed in Eq. (14) and Eq. (15).

Disturbance estimation:

$$\frac{d\hat{h}\left(t\right)}{dt} = l_2(\omega_m - \hat{\omega}_m) = [\varepsilon_3(t)\alpha_1]^2(\omega_m - \hat{\omega}_m) \tag{14}$$

Speed estimation:

$$\frac{d\hat{\omega}_m}{dt} = \hat{h}\left(t\right) + \frac{T_e^*}{J} + l_1(\omega_m - \hat{\omega}_m) = \hat{h}\left(t\right) + \frac{T_e^*}{J} + 2\varepsilon_3(t)\alpha_1(\omega_m - \hat{\omega}_m) \tag{15}$$

It should be noted that the values of η_2 and k in $\varepsilon_3\left(t\right)$ are within the range: $0 < \eta_2 < 1$, $k>1$. When e_ω is small, $\varepsilon_3\left(t\right) \to \left(\eta_2 + 0.5k\right)^{-1}$, thereby reducing the observer's overcompensation for $h(t)$. When e_ω is large (e.g., during sudden loadings), $\varepsilon_3\left(t\right) \to {\eta_2}^{-1}$, accelerates the observer's convergence speed.

From Eq. (14), it can be seen that by integrating the current $(\omega_m - \hat{\omega}_m)$, the next moment's $\hat{h}\left(t\right)$ can be estimated. From Eq. (15), it can be seen that using the current $(\omega_m - \hat{\omega}_m)$, $\hat{h}\left(t\right)$, and T_e^*, the next moment's speed $\hat{\omega}_m$ can be estimated. Therefore, ALDO can be represented as shown in Fig. 4.

Combining Eq. (8) and Eq. (10), the proposed controller ALDO-AM-STSM is given by Eq. (16).

$$\begin{cases} {T_{eo}}^* = J\left[-k_1|e_\omega|^{\frac{1}{2}}sign(e_\omega) - k_2\varepsilon_1\left(t\right)e_\omega + u_1 - \hat{h}\left(t\right)\right] \\ \dfrac{du_1}{dt} = -k_3\varepsilon_2\left(t\right)sign(e_\omega) - k_4\xi e_\omega \end{cases} \tag{16}$$

Stability proof and analysis

When $|{T_e}^*| > |{T_{es}}^*|$, the SynRM speed control system reaches saturation, the output of the speed loop is a constant value. At this point, the stability of the speed control system depends on the stability of the current loop. Since the current loop employs a PI controller, the system remains stable during saturation. When $|{T_e}^*| < |{T_{es}}^*|$, the system is not saturated, and system stability is determined by the speed controller. Since the adaptive terms $\varepsilon_1\left(t\right)$ and $\varepsilon_2\left(t\right)$ are never negative and are less than or equal to η_1^{-1} under all conditions. Therefore, when the system is unsaturated, it is only necessary to prove the stability of the speed controller Eq. (17).

$$\begin{cases} {T_e}^* = J\left[-k_1|e_\omega|^{\frac{1}{2}}sign(e_\omega) - k_2 e_\omega + u_1\right] \\ \dfrac{du_1}{dt} = -k_3 sign(e_\omega) - k_4 e_\omega + \dfrac{d\phi}{dt} \end{cases} \tag{17}$$

Assumption When the disturbance term ϕ satisfies $\left|\frac{d\phi}{dt}\right| \leqslant \theta$ and $\theta>0$, i.e., ϕ is continuously differentiable with bounded first derivatives, and k_1, k_2, k_3, and k_4 satisfy the relationship in Eq. (18), then the speed controller in Eq. (17) meets the Lyapunov conditions for asymptotic stability and converges within a finite time.

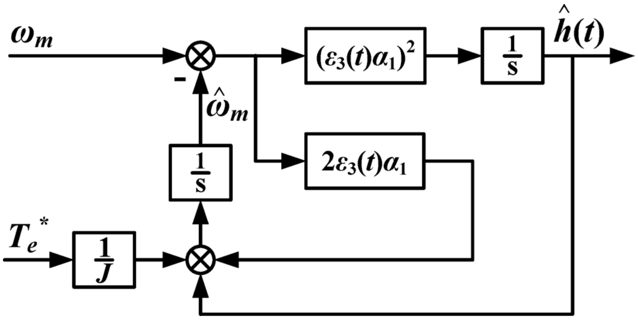

Fig. 4. ALDO Block Diagram.

$$\begin{aligned} & k_1 > (2\theta)^{0.5}, k_2 > 0, k_3 > \theta \\ & k_4 > \frac{8k_2^2k_3 + 9k_1^2k_2^2 + 9\theta^2k_2^2{k_1}^{-2} - 24\theta k_2^2}{4k_3 + 10\theta k_2^2 - 8\theta^2{k_1}^{-2}} \end{aligned} \tag{18}$$

Proof Construct the Lyapunov function shown in Eq. (19).

$$V = 2k_2\left|e_\omega\right| + k_4e_\omega^2 + 0.5u_1^2 + 0.5(k_1|e_\omega|^{0.5}sign\left(e_\omega\right) + k_2e_\omega - u_1)^2 \tag{19}$$

Rewrite Eq. (19) in the form of Eq. (20). Since k_1, k_2, k_3, and k_4 are all larger than zero, V is a positive definite matrix.

$$V = X^{\mathrm{T}}QX \tag{20}$$

In Eq. (20), the vector X and matrix Q can be expressed as:

$$X = \begin{bmatrix} |e_\omega|^{0.5}sign\left(e_\omega\right) \\ e_\omega \\ u_1 \end{bmatrix} = \begin{bmatrix} z_1 \\ z_2 \\ z_3 \end{bmatrix} \quad , \quad Q = \tfrac{1}{2}\begin{bmatrix} k_1^2 + 4k_2 & k_1k_2 & -k_1 \\ k_1k_2 & k_2^2 + 2k_4 & -k_2 \\ -k_1 & -k_2 & 2 \end{bmatrix} \tag{21}$$

Equation (20) satisfies the relationship in Eq. (22). Here, $\|X\|_2$denotes the norm of X, while $\lambda_{1\text{min}}\left\{Q\right\}$ and $\lambda_{1\max}\left\{Q\right\}$ represent the minimum and maximum eigenvalues of matrix Q, respectively, with both $\lambda_{1\text{min}}\left\{Q\right\}$ and $\lambda_{1\max}\left\{Q\right\}$ being greater than zero.

$$\begin{cases} \lambda_{1\text{min}}\left\{Q\right\}\|X\|_2^2 \leqslant V \leqslant \lambda_{1\max}\left\{Q\right\}\|X\|_2^2 \\ \|X\|_2^2 = |z_2| + {z_2}^2 + {z_3}^2 \end{cases} \tag{22}$$

There are $z_1 = z_2|z_1|^{-1}$, ${z_1}^2 = {z_2}^2$, and $|z_1|^{-1} = |z_2|^{-0.5}$ relationships between z_1 and z_2 in vector X. Differentiate vector X and rewrite it in the form of Eq. (23).

$$\begin{cases} \dfrac{dX}{dt} = \dfrac{1}{|z_2|^{0.5}}AX + CX + E\dfrac{d\phi}{dt} \\ \dfrac{dX^{\mathrm{T}}}{dt} = \dfrac{1}{|z_2|^{0.5}}X^{\mathrm{T}}A^{\mathrm{T}} + X^{\mathrm{T}}C^{\mathrm{T}} + E^{\mathrm{T}}\dfrac{d\phi}{dt} \end{cases} \tag{23}$$

In Eq. (23), the matrices A and C and the vector E can be expressed as:

$$A = \tfrac{1}{2}\begin{bmatrix} -k_1 & 0 & 1 \\ 0 & -2k_1 & 0 \\ -2k_3 & 0 & 0 \end{bmatrix} \quad , \quad C = \tfrac{1}{2}\begin{bmatrix} -k_2 & 0 & 0 \\ 0 & -2k_2 & 2 \\ 0 & -2k_4 & 0 \end{bmatrix} \quad , \quad E = \begin{bmatrix} 0 \\ 0 \\ 1 \end{bmatrix} \tag{24}$$

Combining Eq. (23) and differentiating Eq. (20) yields Eq. (25).

$$\begin{aligned} \frac{dV}{dt} &= \frac{dX^{\mathrm{T}}}{dt}QX + X^{\mathrm{T}}Q\frac{dX}{dt} \\ &= \tfrac{1}{|z_2|^{0.5}}\left[X^{\mathrm{T}}A^{\mathrm{T}}QX + X^{\mathrm{T}}QAX\right] + X^{\mathrm{T}}C^{\mathrm{T}}QX + X^{\mathrm{T}}QCX \\ &+ \tfrac{d\phi}{dt}\left(E^{\mathrm{T}}QX + X^{\mathrm{T}}QE\right) \end{aligned} \tag{25}$$

Since $E^{\mathrm{T}}QX = X^{\mathrm{T}}QE$ and ϕ is a bounded constant, Eq. (25) can be rewritten in the form of Eq. (26), where the vector $B = \begin{bmatrix} -k_1 & -k_2 & 2 \end{bmatrix}^{\mathrm{T}}$.

$$\frac{dV}{dt} \leqslant \frac{1}{|z_2|^{0.5}}X^{\mathrm{T}}\left(A^{\mathrm{T}}Q + QA\right)X + X^{\mathrm{T}}\left(C^{\mathrm{T}}Q + QC\right)X + \theta B^{\mathrm{T}}X \tag{26}$$

Define $P = -A^{\mathrm{T}}Q - QA$ and $H = -C^{\mathrm{T}}Q - QC$, and rewrite Eq. (26) in the form of Eq. (27), where $-|z_2|^{-0.5}X^{\mathrm{T}}KX = \theta B^{\mathrm{T}}X$.

$$\frac{dV}{dt} \leqslant -\frac{1}{|z_2|^{\frac{1}{2}}}X^{\mathrm{T}}\left(P + K\right)X - X^{\mathrm{T}}HX \tag{27}$$

Based on matrices A, C, Q, and vector B, matrices P, K, and H in Eq. (27) can be expressed as:

$$P = \tfrac{1}{2}\begin{bmatrix} k_1^3 + 2k_1k_3 & -k_2k_3 + \tfrac{3}{2}k_1^2k_2 & -k_1^2 \\ -k_2k_3 + \tfrac{3}{2}k_1^2k_2 & 4k_1k_4 + 2k_1k_2^2 & -\tfrac{3}{2}k_1k_2 \\ -k_1^2 & -\tfrac{3}{2}k_1k_2 & k_1 \end{bmatrix}$$

$$K = \frac{sign(z_2)}{2}\left[\begin{array}{ccc} 2\theta k_1 & \theta k_2 & -2\theta \\ \theta k_2 & 0 & 0 \\ -2\theta & 0 & 0 \end{array}\right] \quad , \quad H = \frac{1}{2}\left[\begin{array}{ccc} k_1^2 k_2 + 4k_2k_3 & -k_1k_4 + \frac{3}{2}k_1k_2^2 & -\frac{3}{2}k_1k_2 \\ -k_1k_4 + \frac{3}{2}k_1k_2^2 & 2k_2k_4 + 2k_2^3 & -2k_2^2 \\ -\frac{3}{2}k_1k_2 & -2k_2^2 & 2k_2 \end{array}\right] \tag{28}$$

Based on the relationship between z_1 and z_2 and the positive definite matrix property of Eq. (20), Eq. (27) is transformed into the form of Eq. (29), where $-|z_2|^{-0.5}X^{\mathrm{T}}MX = X^{\mathrm{T}}NX$.

$$-\frac{1}{|z_2|^{0.5}}X^{\mathrm{T}}\left(P+K\right)X - X^{\mathrm{T}}HX = -\frac{1}{|z_2|^{0.5}}X^{\mathrm{T}}\left(P+K+M\right)X - X^{\mathrm{T}}\left(H+N\right)X \tag{29}$$

In Eq. (29), matrices *M* and *N* are expressed as follows:

$$M = \frac{1}{2}\left[\begin{array}{ccc} 0 & k_2k_3 - \frac{3}{2}k_1^2k_2 & 0 \\ k_2k_3 - \frac{3}{2}k_1^2k_2 & -2k_1k_4 + 3k_1k_2^2 & -\frac{3}{2}k_1k_2 \\ 0 & -\frac{3}{2}k_1k_2 & 0 \end{array}\right] \quad , \quad N = \frac{1}{2}\left[\begin{array}{ccc} -2k_2k_3 + 3k_1^2k_2 & k_1k_4 - \frac{3}{2}k_1k_2^2 & \frac{3}{2}k_1k_2 \\ k_1k_4 - \frac{3}{2}k_1k_2^2 & 0 & 0 \\ \frac{3}{2}k_1k_2 & 0 & 0 \end{array}\right] \tag{30}$$

Combining matrices *M* and *N*, matrices *P* and *H* can be simplified to:

$$P = \frac{1}{2}\left[\begin{array}{ccc} k_1^3 + 2k_1k_3 & 0 & -k_1^2 \\ 0 & 2k_1k_4 + 5k_1k_2^2 & -3k_1k_2 \\ -k_1^2 & -3k_1k_2 & k_1 \end{array}\right] \quad , \quad H = \left[\begin{array}{ccc} 2k_1^2k_2 + k_2k_3 & 0 & 0 \\ 0 & k_2k_4 + k_2^3 & -k_2^2 \\ 0 & -k_2^2 & k_2 \end{array}\right] \tag{31}$$

When $P+K>0, H>0$, there exists $\frac{dV}{dt}<0$ satisfying Lyapunov stability condition, the stability condition for the speed control system can be given by Eq. (32).

$$\begin{aligned} & k_1 > (2\theta)^{0.5}, k_2 > 0, k_3 > \theta \\ & k_4 > \frac{8k_2^2k_3 + 9k_1^2k_2^2 + 9\theta^2k_2^2k_1^{-2} - 24\theta k_2^2}{4k_3 + 10\theta k_2^2 - 8\theta^2 k_1^{-2}} \end{aligned} \tag{32}$$

When k_1, k_2, k_3, and k_4 satisfy Eq. (32), the eigenvalues of matrices $P+K$ and H are both greater than zero. Therefore, combining with Eq. (22) yields the relationship in Eq. (33). Here, $\lambda_{1\min}\{P+K\}$ and $\lambda_{1\min}\{H\}$ denote the minimum eigenvalues of matrices$P+K$ and H, respectively, with $\lambda_{1\min}\{P+K\}>0$ and $\lambda_{1\min}\{H\}>0$.

$$\frac{dV}{dt} \leqslant -\frac{1}{|z_2|^{0.5}}\lambda_{1\min}\{P+K\}\left\|X\right\|_2^2 - \lambda_{1\min}\{H\}\left\|X\right\|_2^2 \tag{33}$$

Equation (22) satisfies the relationship $|z_2|^{0.5} \leqslant \left\|X\right\|_2 \leqslant V^{0.5}\lambda_{1\min}^{-0.5}\{Q\}$. Combined with $V \leqslant \lambda_{1\max}\{Q\}\left\|X\right\|_2^2$, this further yields the relationship in Eq. (34).

$$\begin{cases} \frac{1}{|z_2|^{0.5}}\left\|X\right\|_2^2 \geqslant \frac{\lambda_{1\min}^{0.5}\{Q\}}{V^{0.5}} \cdot \frac{V}{\lambda_{1\max}\{Q\}} \\ \lambda_{1\min}\{H\}\left\|X\right\|_2^2 \geqslant \lambda_{1\min}\{H\}\frac{V}{\lambda_{1\max}\{Q\}} \end{cases} \tag{34}$$

Combining Eq. (33) and Eq. (34) yields the relationship in Eq. (35).

$$\begin{cases} \frac{dV}{dt} \leqslant -\delta_1 V^{0.5} - \delta_2 V \\ \delta_1 = \frac{\lambda_{1\min}\{P+K\}\lambda_{1\min}^{0.5}\{Q\}}{\lambda_{1\max}\{Q\}} > 0, \delta_2 = \frac{\lambda_{1\min}\{H\}}{\lambda_{1\max}\{Q\}} > 0 \end{cases} \tag{35}$$

Since both δ_1 and δ_2 are greater than zero in Eq. (35), it follows that Eq. (17) converges to zero in finite time. Thus, the hypothesis is proven.

Current loop design

After the speed loop calculates the desired torque $T_{eo}{}^*$, it serves as the input to the current loop. The current loop converts $T_{eo}{}^*$ into the desired stator current based on the selected control strategy. As shown by the electromagnetic torque equation in Eq. (3), an infinite number of current possibilities exist for a given $T_{eo}{}^*$. To obtain the minimum stator current i_s among them; this paper adopts the MTPA vector control strategy. This strategy aims to generate the required electromagnetic torque output using the smallest possible i_s, which can be equivalently formulated as solving the extremum problem of Eq. (36).

$$\begin{cases} \text{constant}: T_e = \frac{3}{2}p_n\left(L_d - L_q\right)i_d i_q \\ \min: i_s^2 = {i_d}^2 + {i_q}^2 \end{cases} \tag{36}$$

To further compute i_d and i_q in Eq. (36), we construct the auxiliary function Eq. (37), where μ is the Lagrange multiplier.

$$K\left(i_d, i_q, \mu\right) = {i_d}^2 + {i_q}^2 + \mu[T_e^* - \frac{3}{2} p_n \left(L_d - L_q\right) i_d i_q] \tag{37}$$

For Eq. (37), find the partial derivatives of i_d, i_q, and μ, and set the partial derivatives equal to zero, yielding the relationship in Eq. (38).

$$\begin{cases} \dfrac{\partial K}{\partial i_d} = 2 i_d - \dfrac{3}{2} \mu p_n (L_d - L_q) i_q = 0 \\ \dfrac{\partial K}{\partial i_q} = 2 i_q - \dfrac{3}{2} \mu p_n (L_d - L_q) i_d = 0 \\ \dfrac{\partial K}{\partial \mu} = T_e - \dfrac{3}{2} p_n (L_d - L_q) i_d i_q = 0 \end{cases} \tag{38}$$

Solving the first two equations of Eq. (38) yields the relationship $i_d = \pm i_q$. Substituting this into the third equation of Eq. (38) provides the desired currents i_q^* and i_d^* for the current loop, as shown in Eq. (39).

$$\begin{cases} i_q^* = i_d^*, \quad T_{eo}^* > 0 \\ i_d^* = \sqrt{\dfrac{T_{eo}^*}{1.5 p_n \left(L_d - L_q\right)}} \end{cases} \text{and} \quad \begin{cases} i_q^* = -i_d^*, \quad T_{eo}^* < 0 \\ i_d^* = \sqrt{\dfrac{-T_{eo}^*}{1.5 p_n \left(L_d - L_q\right)}} \end{cases} \tag{39}$$

Simulation verification and analysis

To investigate the performance of the SynRM speed control system based on ALDO-AM-STSM, a corresponding simulation system was established in Matlab/Simulink, as shown in Fig. 5. In the simulation model, the solver was configured as a fixed-step discrete system without continuous states, with a step size T_s = 1e-6 s. The sampling time for current, torque, and electrical angle was set to T_{pwm} = 1e-5 s, while the speed sampling time was 10 times T_{pwm} to simulate the 10 kHz switching frequency of the experimental equipment. The speed loop comprises an AM-STSM controller and an ALDO. The AM-STSM block generates the desired torque value T_e^* (without disturbance consideration) based on speed deviation. This T_e^* undergoes feedforward compensation via the ALDO stage to yield the desired torque value ${T_{eo}}^*$ (with disturbance consideration). The ${T_{eo}}^*$ serves as the input to the current control module, where the MTPA current control unit solves for i_d^* and i_q^* according to Eq. (39). Finally, the current loop combines PI control with voltage compensation to enable the actual current to rapidly track i_d^* and i_q^*.

The design values in AM-STSM are $k_1 = 350$, $k_2 = 45$, $k_3 = 5000$, $k_4 = 35$, and $\eta_1 = 0.6$, which clearly satisfy the stability condition of Eq. (32). The design values in ALDO are $\eta_2 = 0.5$, $k = 9$, and $\alpha_1 = 750$. The parameters of the d-q axis current PI controller in the current loop are designed as K_{pd} = 226.08, K_{pq} = 108.6, and K_{id} = K_{iq} = 3756.6. The SynRM parameters used in the simulation are listed in Table 1.

The gain trajectories of the adaptive terms $\varepsilon_1(t)$, $\varepsilon_2(t)$, and $\varepsilon_3(t)$ in Eq. (6) and Eq. (13) are shown in Fig. 6. During no-load startup and sudden load application, the angular velocity error $|e_\omega|$ is large, causing the system trajectory to deviate significantly from the sliding surface. The $\varepsilon_1(t)$ and $\varepsilon_2(t)$ terms increase and approach η_1^{-1} (approximately 1.67), enabling the system to rapidly converge toward the sliding surface ($s = 0$). At this point, $\varepsilon_3(t)$ approaches 2, accelerating the convergence of the observed values. After system stabilization, $\varepsilon_1(t)$, $\varepsilon_2(t)$, and $\varepsilon_3(t)$ converge to 0, 1, and 0.2 respectively, effectively suppressing chattering after reaching

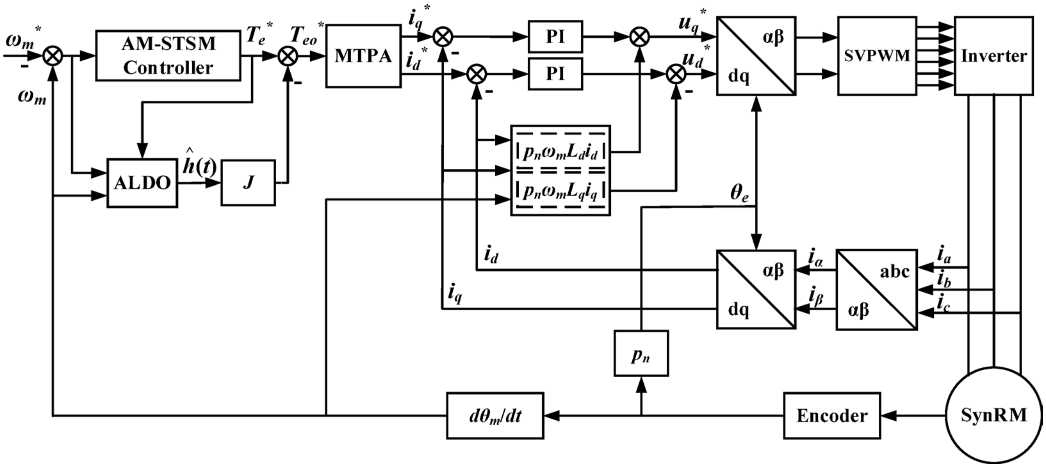

Fig. 5. Block Diagram of the Speed Control System for the SynRM.

Parameter	Unit	Value
Rated power	kW	1.1
Rated speed	r/min	1500
Rated torque	N m	7
Pole pairs/p_n	–	2
Stator resistance/R_s	Ω	5.5
D-axis inductance/L_d	H	0.331
Q-axis inductance/L_q	H	0.159
Moment of inertia/J	kg m^2	0.0034

Table 1. Parameters of SynRM.

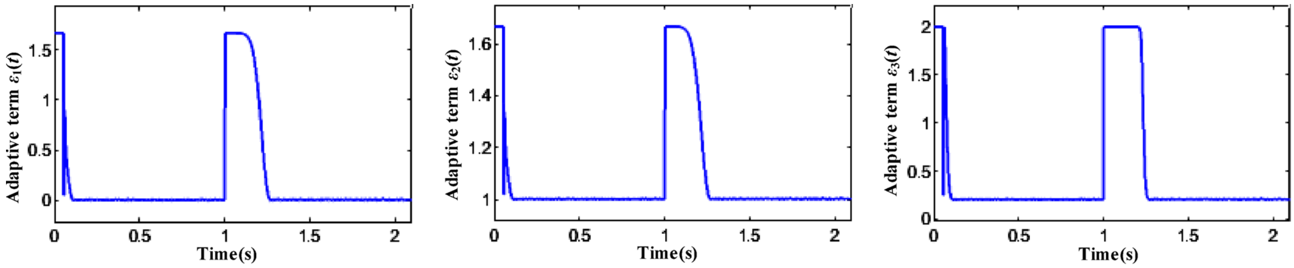

(a) $\varepsilon_1(t)$ (b) $\varepsilon_2(t)$ (c) $\varepsilon_3(t)$

Fig. 6. Adaptive term gain value trajectory.

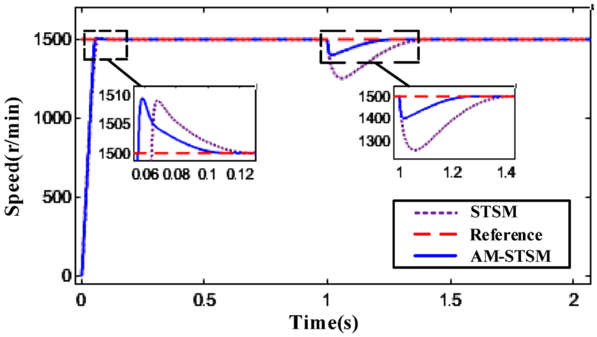

Fig. 7. Speed Response of AM-STSM Controller and STSM Controller.

the sliding surface. The observer gain α_1 is reduced to 150 to minimize fluctuations in the observed values after stabilization, meeting the design requirements for the adaptive terms.

The speed response curves for AM-STSM and STSM are shown in Fig. 7. During no-load startup, both control schemes exhibit approximately 10 r/min of overshoot, converging to the desired speed at 0.1 s and 0.13 s, respectively. However, AM-STSM demonstrates faster convergence and response speeds. To evaluate anti-disturbance capabilities, a sudden 7 N·m load was applied at 1 s. STSM dropped from 1500 r/min to 1250 r/min, exhibiting a 250 r/min drop (16.67% drop) and recovered to the setpoint within 0.4 s. However, the AM-STSM reduced the drop by 150 r/min (a decrease by 60%) and shortened the recovery time by approximately 38%.

The electromagnetic torque response of the speed control system is shown in Fig. 8. During no-load startup, the torque output of both control schemes is limited to 10.5 N·m, approximately 1.5 times the rated torque. As shown in Fig. 8a, during startup, the AM-STSM system exhibits adaptive capabilities, resulting in a higher current sliding mode control gain. This causes the electromagnetic torque to reach the limit value, enabling rapid startup. When the no-load speed exceeds the desired, the AM-STSM's sliding-mode gain rapidly decreases, significantly suppressing chattering near the sliding surface ($s = 0$) and quickly entering a stable state, concluding the start-up. As shown in Fig. 8b, after applying a sudden 7 N·m load at 1 s, the STSM's torque output peaks at 7.45 N·m and stabilizes around 1.4 s. The AM-STSM achieves a maximum torque output of 7.2 N·m, stabilizing around 1.23 s. After stabilization, both controllers exhibit minor ripples of 0.1 N·m. Simulation results demonstrate that the AM-STSM exhibits smaller overshoot, faster response, and faster convergence speed.

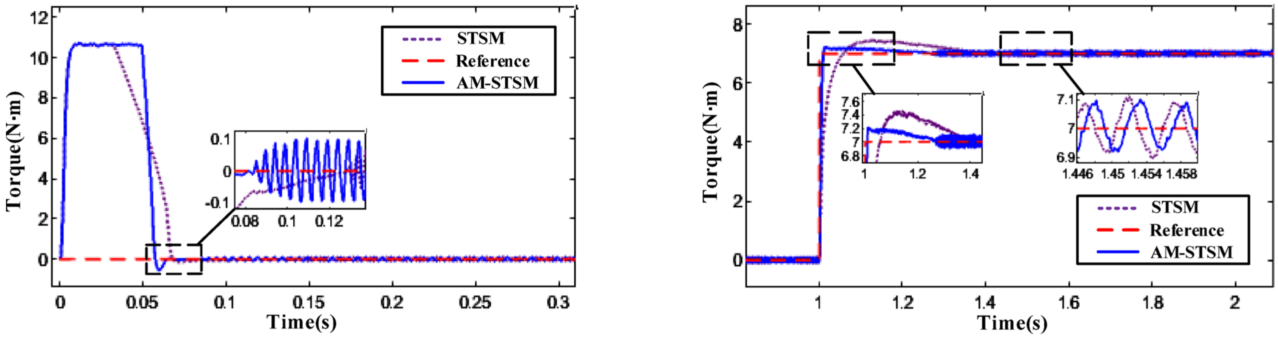

(a) No-load start

(b) Sudden load

Fig. 8. Electromagnetic Torque Response of AM-STSM Controller and STSM Controller. (a) No-load start, (b) Sudden load.

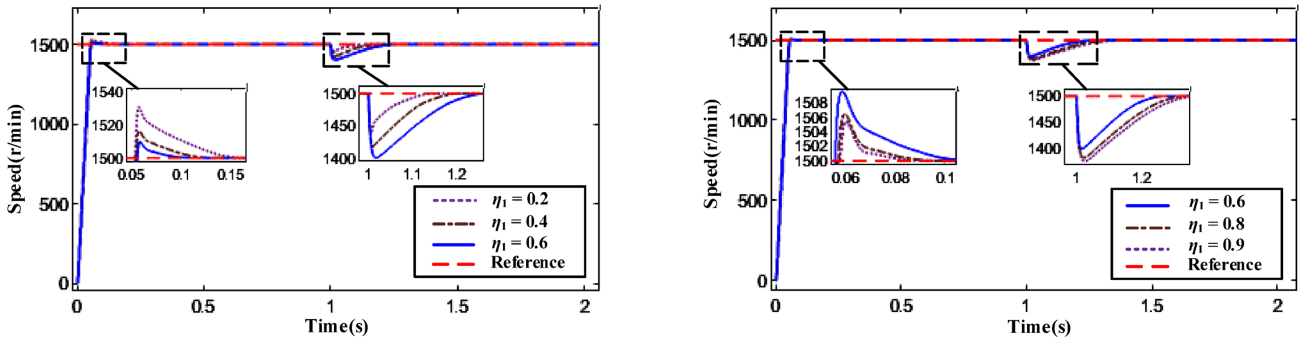

(a) $\eta_1 = 0.2, 0.4, 0.6$

(b) $\eta_1 = 0.6, 0.8, 0.9$

Fig. 9. Effect of Adaptive Item amplification factor η_1^{-1} on speed. (**a**) $\eta_1 = 0.2, 0.4, 0.6$, (**b**) $\eta_1 = 0.6, 0.8, 0.9$.

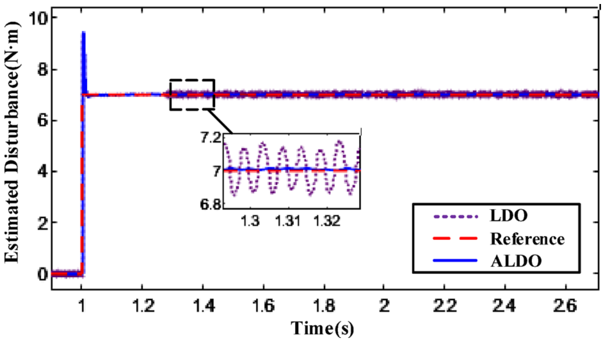

Fig. 10. Observed Values of ALDO and LDO for Lumped Disturbances.

To investigate the impact of the adaptive amplification factor η_1^{-1} on the performance of the speed control system, simulations were conducted under no-load start and sudden load application (7 N·m) conditions while keeping all other parameters constant and varying only η_1, as shown in Fig. 9. When $\eta_1 = 0.9$, the speed overshoot during no-load start-up is minimal, approximately 5 r/min (0.33% overshoot), while the speed drop during sudden load application is most significant, approximately 100 r/min (6.67% drop). When $\eta_1 = 0.2$, the speed drop during sudden load application was minimal, approximately 55 r/min (3.67% drop), but the overshoot during no-load start was maximum, approximately 30 r/min (2% overshoot). Simulation data indicates that reducing η_1 enhances the system's resistance to load disturbances but increases overshoot during no-load starts. Therefore, the η_1 value should be selected based on actual requirements.

A comparison of disturbance observations between ALDO and LDO is shown in Fig. 10. The initial α_1 values for the two observers were set to 750 and 1500, respectively. When disturbances are present, ALDO's adaptive term amplifies α_1 to 1500, resulting in identical gain matrix values. Therefore, when a 7 N·m load is suddenly

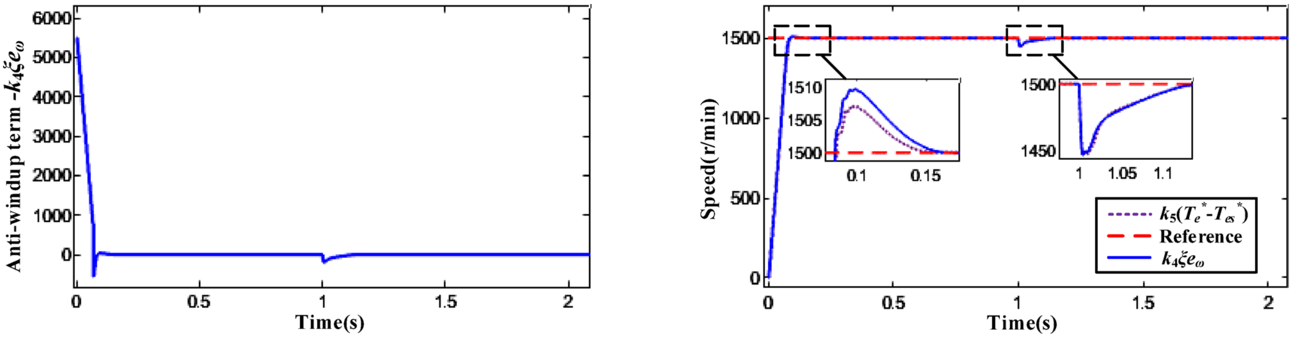

(a) Anti-windup Strategy Validation (b) Comparison of Two Anti-windup Strategies

Fig. 11. Anti-windup Strategy Validation and Comparison. (**a**) Anti-windup Strategy Validation, (**b**) Comparison of Two Anti-windup Strategies.

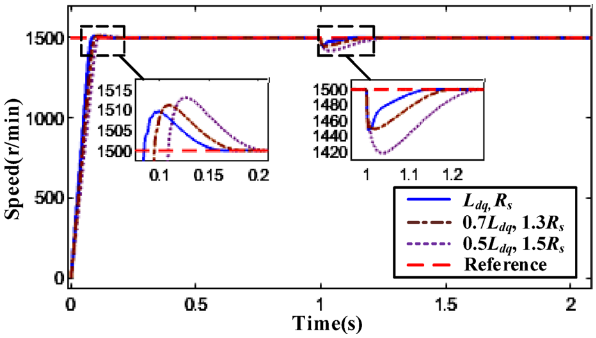

Fig. 12. Impact of mismatch in resistive and inductive parameters on control performance.

applied at 1 s, both observers exhibit the same overshoot of approximately 2.5 N·m (35.71% overshoot). After the rotational speed stabilizes, ALDO's adaptive term reduces α_1 to 150, resulting in smaller fluctuations in ALDO's observed values and significantly improving observation accuracy.

The trajectory of the anti-windup term in Eq. (16) is shown in Fig. 11a. During the motor start-up phase, the $-k_4\xi e_\omega$ term is a large positive value, enabling the integral term to rapidly exit saturation. After exiting saturation, the $-k_4\xi e_\omega$ term becomes negative to accelerate the elimination of steady-state speed error. Rewriting the derivative term in Eq. (16) as $-k_3\varepsilon_2\,(t)\,sign(e_\omega) - k_4 e_\omega + k_5\,(T_e^* - T_{es}^*)$ yields the standard anti-windup method described in reference[34]. A comparison of the speed response between this method and the proposed anti-windup strategy is shown in Fig. 11b. When k_5 is appropriately designed, both strategies exhibit comparable performance in terms of speed overshoot and recovery time.

During motor operation, parameter shifts may occur. A comparison of speed responses under inductance-resistance parameter mismatches is shown in Fig. 12. The inductance and resistance parameters of the motor model were varied from (L_{dq}, R_s) to ($0.7L_{dq}$, $1.3R_s$) and ($0.5L_{dq}$, $1.5R_s$), respectively. Figure 12 shows that when the parameter mismatch is small, there are no significant changes in the overshoot during startup, the speed drop under sudden load, or the speed stabilization time. When the parameter mismatch is significant, the speed overshoot during startup increases by 5 r/min (increase of 50%), and the speed drop under a sudden 7 N·m load increases by 20 r/min (increase of 50%). Both increases are relatively small. This demonstrates that the ALDO-AM-STSM exhibits good parameter robustness.

To investigate the impact of ALDO on the system, the speed responses of ALDO-AM-STSM and AM-STSM (without ALDO) were compared as shown in Fig. 13. After the sudden load application (7 N·m), the speed drop of ALDO-AM-STSM was smaller, amounting to 60 r/min (a 60% reduction compared to AM-STSM), and it recovered to the desired speed within 0.35 s. At 1.3 s after load unloading, ALDO-AM-STSM exhibited a smaller overshoot (approximately 25 r/min, 1.67% overshoot) and shorter recovery time. Results indicate that compared to AM-STSM, ALDO-AM-STSM demonstrates superior performance in both speed drop and recovery time.

Experimental validation and analysis

The SynRM controller's hardware utilizes the TMS320F28335 as its main control chip, implementing the previously discussed control algorithms as software programs. To investigate the experimental characteristics of SynRM speed control, a hysteresis brake was employed to apply a load to the motor, capable of exerting up to 10 N·m. The constructed experimental platform is shown in Fig. 14, where the hysteresis brake, dynamic torque sensor, and motor rotate coaxially during operation. Speed information is obtained from an optoelectronic

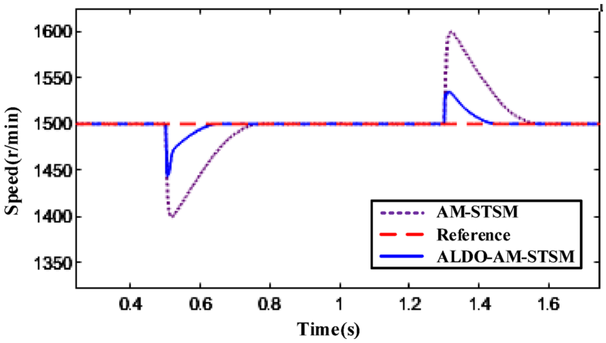

Fig. 13. Load Sudden Change Speed Response Curve.

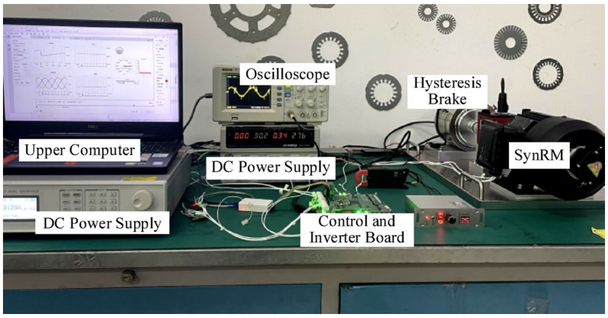

Fig. 14. SynRM Speed Control Experimental Platform.

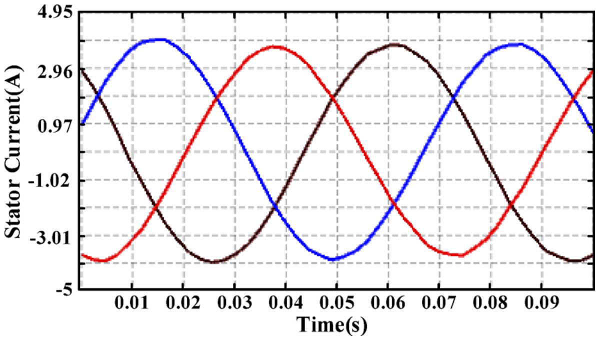

Fig. 15. Three-phase stator current during stable operation.

encoder with a resolution of 3600 pulses per revolution. Three-phase current information is obtained after processing by the AD7616 chip, which has a resolution of 16 bits. The dynamic torque sensor displays the real-time load value applied by the brake, along with the motor speed and power output. The inverter switch's PWM interrupt frequency is 10 kHz. Sampling times for current, electrical angle, and speed match those set in the simulation (speed sampling interval: 1 ms; current and electrical angle sampling interval: 0.1 ms).

During the experiment, the relevant parameters in the AM-STSM were set as follows: $k_1 = 20$, $k_2 = 26$, $k_3 = 0.65$, $k_4 = 0.0016$, and $\eta_1 = 0.6$. The corresponding parameters in ALDO were set as: $\eta_2 = 0.5$, $k = 9$, $\alpha_1 = 0.075$. Among them, k_3, k_4, and α_1 are all parameter values after integral discretization multiplied by 10 times T_{pwm}. The integral and proportional terms in STSM were identical to those in AM-STSM. The speed was uniformly set to 1000 r/min during the experiments.

At a load value of 5 N·m, the three-phase stator currents after motor stabilization are shown in Fig. 15. The current waveforms are essentially sinusoidal with an amplitude of approximately 3.95 A. The disturbance observation values of the control system are depicted in Fig. 16. A disturbance of 5.5 N·m was applied at 5.5 s, and the stabilized ALDO observation value was approximately 5.6 N·m, slightly higher than the actual value. Experiments demonstrate that ALDO can effectively track lumped disturbances.

A comparison of stator current waveforms using MTPA and non-MTPA ($i_d^* = 0.4\left|T_{eo}{}^*\right|,\ i_q^* = T_{eo}{}^*$) current control is shown in Fig. 17. After no-load start-up speed stabilization, the current consumption of both

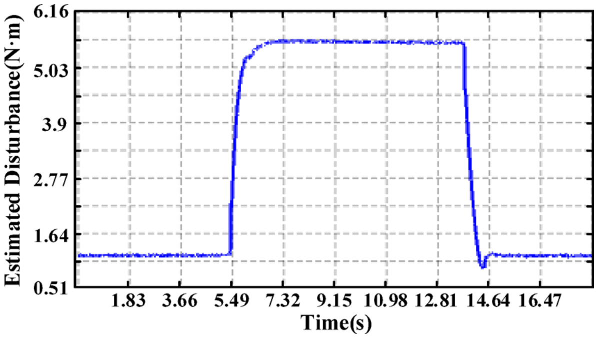

Fig. 16. Lumped disturbance observation value.

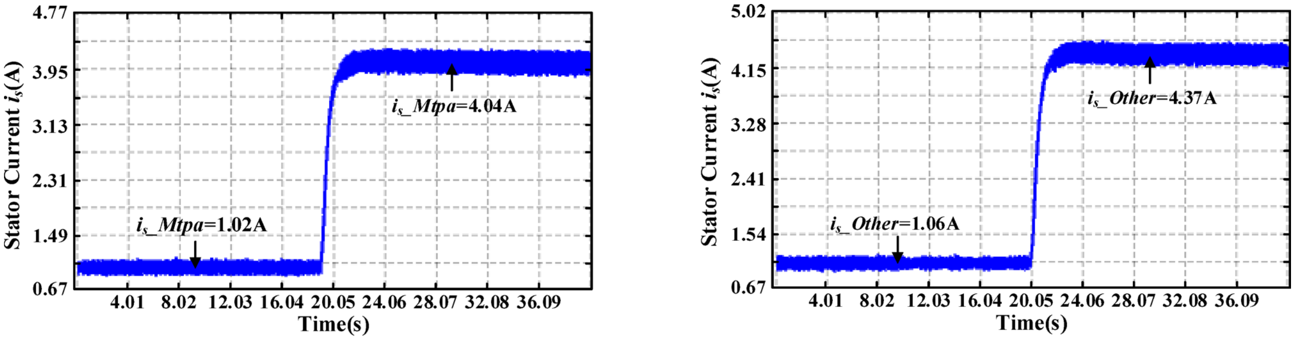

(a) MTPA Control

(b) Non-MTPA control

Fig. 17. Stator Current Waveforms for Different Current Distribution Strategies. (**a**) MTPA Control, (**b**) Non-MTPA control.

current allocation strategies is essentially identical. Under a 5 N·m load, the average stator current of the system employing the MTPA current allocation strategy is lower than that of the non-MTPA control (reduced by 0.33 A), consistent with theoretical analysis.

During no-load startup, the speed and current response curves for the three speed control schemes (Scheme 1: ALDO-AM-STSM; Scheme 2: AM-STSM; Scheme 3: STSM) are shown in Fig. 18, with corresponding data listed in Table 2. Compared to the other two schemes, Scheme 3 exhibits the smallest peak starting current. After stabilization, all three control schemes exhibit good current sinusoidal quality. Regarding overshoot, Scheme 2 and Scheme 3 are comparable, with overshoots of approximately 10 r/min and 9 r/min, respectively. Scheme 1 exhibits a larger starting current due to the $T_{eo}{}^{*}$ supplied to the MTPA during the initial startup phase, which results from the superposition of the disturbance observer and sliding mode controller components. Consequently, Scheme 1 demonstrates a slightly larger overshoot of approximately 34 r/min. Schemes 1 and 2 stabilized at the set speed in 0.52 s and 0.56 s, respectively, both converging faster than Scheme 3 (Scheme 1 is 7.14% faster than Scheme 2 and 21.21% faster than Scheme 3.).

The response curves for rotational speed, electromagnetic torque, and stator current during 2 N·m load startup are shown in Fig. 19. During load startup, no overshoot was observed in any of the three control schemes. After speed stabilization, all schemes exhibited minor fluctuations of approximately ± 1.5 r/min, with good sinusoidal phase current waveforms. Among the three control schemes, Scheme 1 achieved the shortest convergence time of approximately 0.63 s. Scheme 3 produced the smallest torque peak. Following speed stabilization, all three control methods exhibited torque ripples of approximately 0.3 N·m.

The response to sudden load changes during operation is shown in Fig. 20, with corresponding data listed in Table 3. After applying a sudden load (5 N·m), Schemes 1, 2, and 3 exhibited speed reductions of approximately 43 r/min, 102 r/min, and 248 r/min, respectively. Scheme 1 demonstrated the smallest reduction and the shortest time to recover to the desired speed. Compared to scheme 3, scheme 1 reduces speed drop by 82.67% and adjustment time by 47.96%. Compared to scheme 2, it reduces speed drop by 57.84% and adjustment time by 17.95%. After speed stabilization, all three control schemes exhibited approximately 0.8 N·m (15%) of torque ripple. After sudden load removal, Scheme 1 demonstrated the smallest speed overshoot and fastest convergence speed. Compared to Scheme 2 and Scheme 3, Scheme 1 reduced overshoot by 61.09 r/min (decreased by 66.49%) and 247.74 r/min (decreased by 88.95%), respectively, while shortening convergence time by 0.17 s and 0.69 s, respectively. Scheme 1 demonstrated superior anti-disturbance capability.

Based on the combined results of no-load start, load start, and anti-disturbance tests, it is evident that applying the ALDO-AM-STSM controller to SynRM speed control delivers superior recovery characteristics and anti-

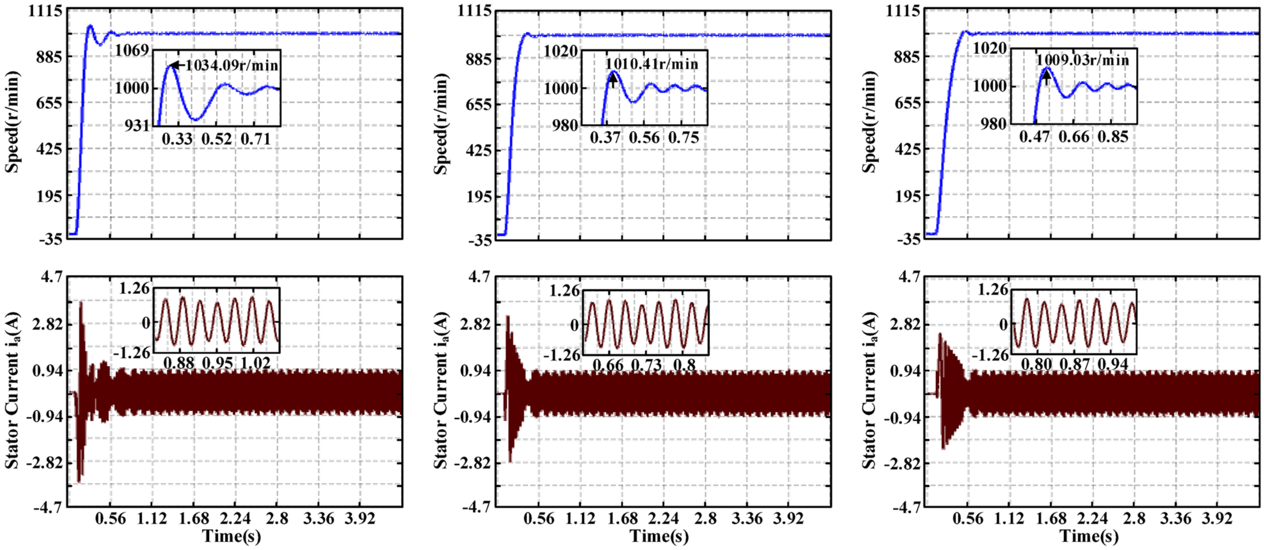

(a) ALDO-AM-STSM (b) AM-STSM (c) STSM

Fig. 18. No-Load Start-Up Experiment. (**a**) ALDO-AM-STSM, (**b**) AM-STSM, (**c**) STSM.

Control method	Peak speed (r/min)	Speed overshoot (r/min)	Adjustment time (s)	Peak starting current (A)
Scheme 1	1034.09	34.09	0.52	3.76
Scheme 2	1010.41	10.41	0.56	3.26
Scheme 3	1009.03	9.03	0.66	2.5

Table 2. No-load startup experimental data.

disturbance capability. These properties are particularly crucial for electric vehicle applications. For instance, during overtaking maneuvers or hill climbs, the drive motor faces sudden torque demands. This solution ensures smooth speed transitions, eliminating jerky sensations to enhance ride comfort and safety. Simultaneously, when robotic arms grasp workpieces, it guarantees stable operation, preventing vibrations or positioning errors caused by abrupt load changes.

Conclusions

This paper proposes a composite control scheme combining adaptive multivariable super-twisting sliding mode (AM-STSM) control with an adaptive Luenberger disturbance observer (ALDO) to enhance the dynamic and anti-disturbance performance of the SynRM speed control system. Through theoretical analysis, simulation studies, and experimental validation, the following conclusions are obtained:

1) The proposed AM-STSM controller effectively balances the trade-off between system response speed and steady-state accuracy through an adaptive gain scheme. The adaptive terms $\varepsilon_1\,(t)$ and $\varepsilon_2\,(t)$ dynamically adjust gains based on rotational speed error, enabling strong convergence during startup and large disturbance phases while smoothly suppressing sliding mode chattering as steady-state approaches.
2) The designed ALDO achieves high-precision observation and real-time compensation for lumped disturbances. Its adaptive gain $\varepsilon_3\,(t)$ ensures rapid response during dynamic processes and smooth decay in steady-state phases, thereby enhancing system robustness while avoiding excessive observation noise.
3) Simulation and experimental results demonstrate that compared to traditional STSM, ALDO-AM-STSM achieves shorter adjustment times during no-load startup, but with a slight increase in speed overshoot. Under sudden load additions, it reduces speed drop by 82.67% and shortens adjustment time by approximately 47.96%. During sudden load shedding, it reduces speed overshoot by 88.95% and shortens regulation time by approximately 50.36%, while significantly reducing steady-state torque and speed fluctuations.

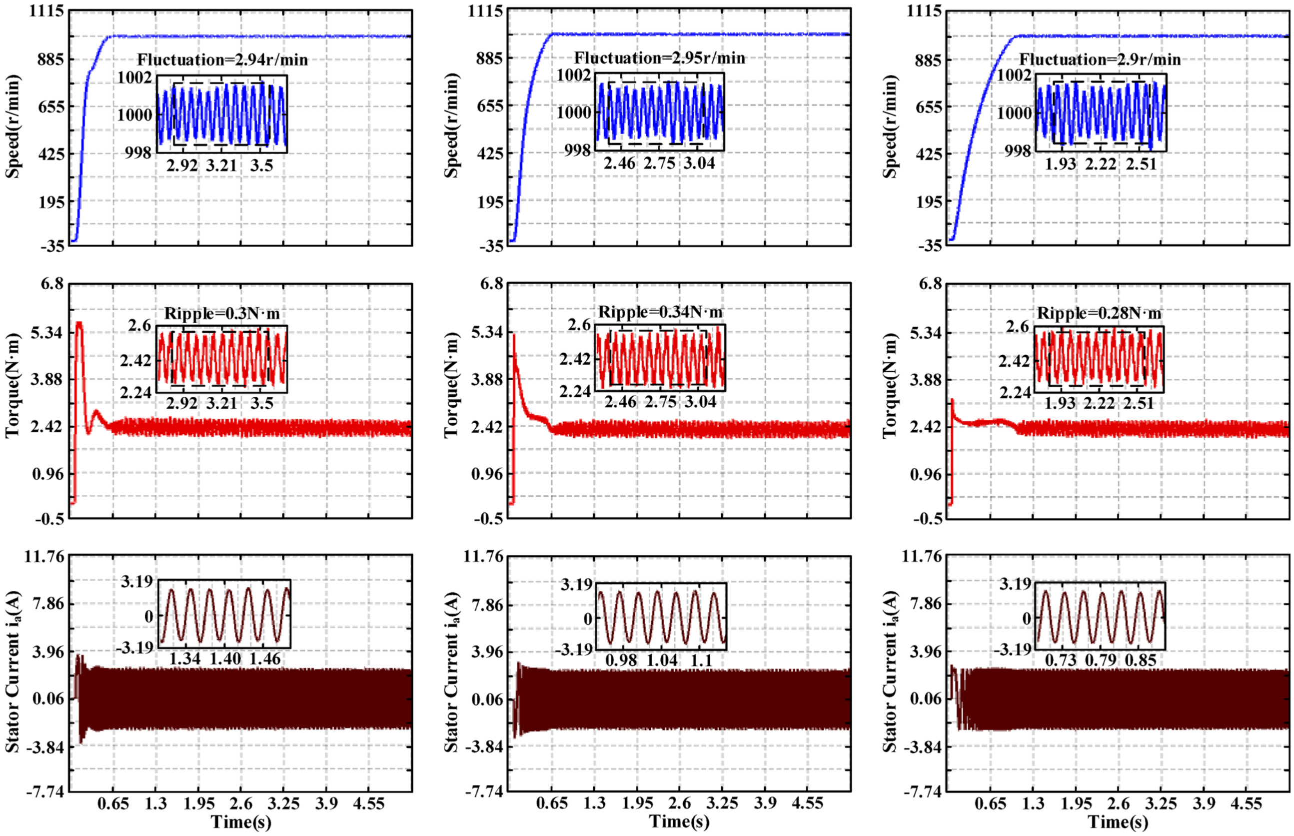

(a) ALDO-AM-STSM (b) AM-STSM (c) STSM

Fig. 19. Load Start-up Experiment. (**a**) ALDO-AM-STSM, (**b**) AM-STSM, (**c**) STSM.

ALDO-AM-STSM provides an effective solution for addressing chattering and anti-disturbance issues in SynRM speed control systems, significantly enhancing the system's dynamic and static performance as well as control quality. Compared to nonlinear control strategies such as model predictive control, feedback linearization, and nonlinear optimal control, ALDO-AM-STSM requires lower model accuracy, imposes a lighter computational burden, and is simpler to implement. However, further research will be conducted on the parameter system adjustment of this strategy, the mismatch perturbation caused parameter mismatches, and control adaptability issues during wide speed range operation.

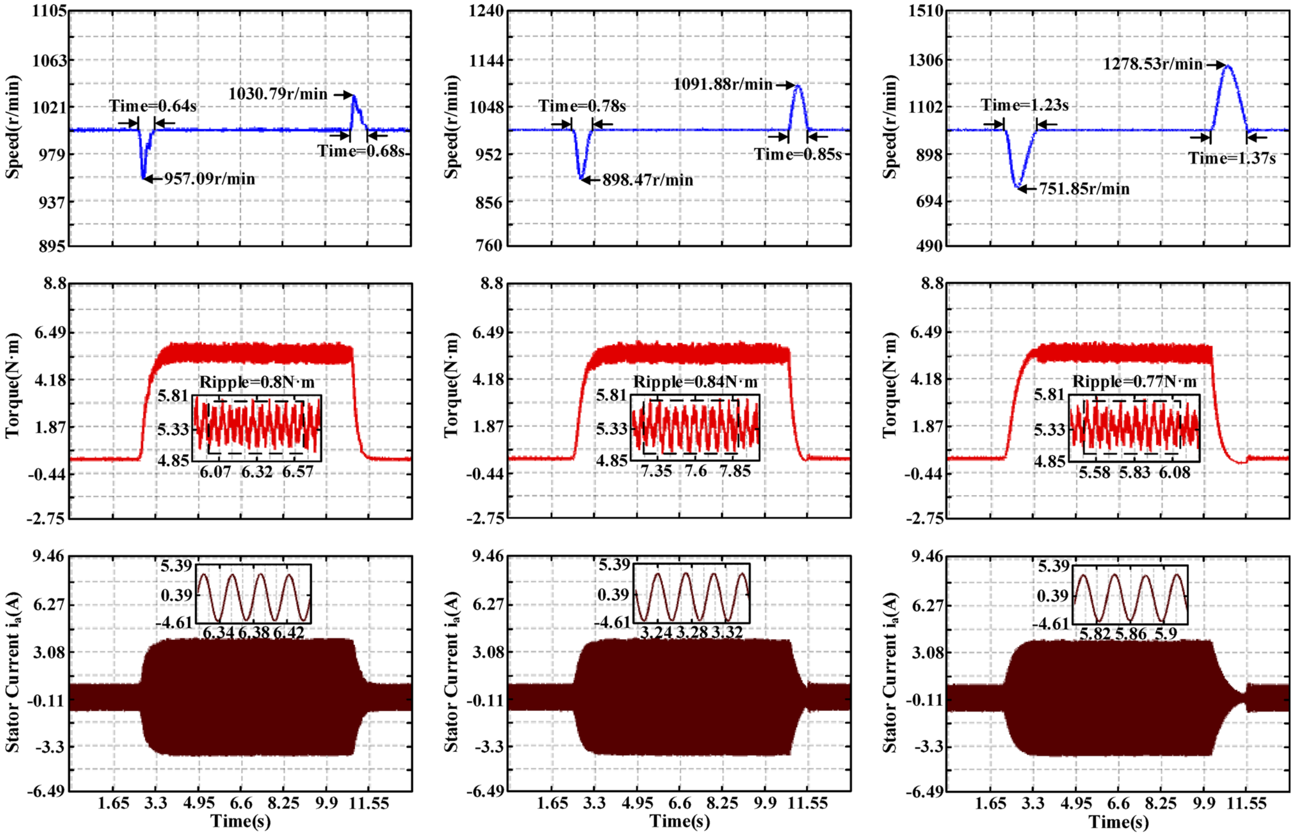

(a) ALDO-AM-STSM (b) AM-STSM (c) STSM

Fig. 20. Anti-disturbance Performance Experiment. (**a**) ALDO-AM-STSM, (**b**) AM-STSM, (**c**) STSM.

Control method	Maximum drop (r/min)	Adjustment time (s)	Maximum overshoot (r/min)	Adjustment time (s)
Scheme 1	43	0.64	31	0.68
Scheme 2	102	0.78	92	0.85
Scheme 3	248	1.23	279	1.37

Table 3. Anti-disturbance experimental data.

Data availability

All data generated or analysed during this study are included in this published article.

Received: 1 September 2025; Accepted: 5 December 2025

References

1. AngayarKanni, S., Kumar, K. R. & Senthilnathan, A. Comprehensive overview of modern controllers for synchronous reluctance motor, *Journal of Electrical and Computer Engineering*, Vol. No. 1, 1345792, 2023. (2023).
2. Kim, K. C., Ahn, J. S., Won, S. H., Hong, J. P. & Lee, J. A study on the optimal design of synrm for the high torque and power factor. *IEEE Trans. Magn.* **43** (6), 2543–2545 (June 2007).
3. Zhang, S. et al. Shape Design Optimization and Comparative Analysis of a Novel Synchronous Reluctance Machine With Grain-Oriented Silicon Steel, *IEEE Transactions on Magnetics*, Vol. 60, No. 9, 1–5, Sept. (2024).
4. Murataliyev, M., Degano, M., Di Nardo, M., Bianchi, N. & Gerada, C. Synchronous Reluctance Machines: A Comprehensive Review and Technology Comparison, *Proceedings of the IEEE*, Vol. 110, No. 3, 382–399, March 2022.
5. Farhan, A., Abdelrahem, M., Saleh, A., Shaltout, A. & Kennel, R. Jan., Simplified sensorless current predictive control of synchronous reluctance motor using online parameter Estimation. *Energies*, **13**, 492, (2020).
6. Hadla, H. & Santos, F. Performance comparison of Field-oriented control, direct torque control, and Model-predictive control for synrms. *Chinese J. Electr. Engineering*, **8**, 1, 24–37, March 2022.
7. Nikmaram, B. et al. Oct., Full-Cycle Iterative Observer: A Comprehensive Approach for Position Estimation in Sensorless Predictive Control of SynRM, *IEEE Journal of Emerging and Selected Topics in Power Electronics*, Vol. 8 12, No. 5, 5246–5257, (2024).

8. Chen, S. G., Lin, F. J., Liang, C. H. & Liao, C. H. Intelligent maximum power factor searching control using recurrent Chebyshev fuzzy neural network current angle controller for synrm drive system. *IEEE Trans. Power Electronics*, **36**, 3, 3496–3511, March 2021.
9. Hou, Q., Ding, S., Yu, X. & Mei, K. A Super-Twisting-Like Fractional Controller for SPMSM Drive System, *IEEE Transactions on Industrial Electronics*, Vol. 69, No. 9, 9376–9384, Sept. (2022).
10. Accetta, A., Cirrincione, M., D'Ippolito, F., Pucci, M. & Sferlazza, A. Robust Control of Synchronous Reluctance Motor Based on Automatic Disturbance Rejection, *IEEE Open Journal of Industry Applications*, Vol. 5, 209–223, May. (2024).
11. Accetta, A., Cirrincione, M., Pucci, M. & Sferlazza, A. Feedback linearization based nonlinear control of synrm drives accounting for Self- and Cross-Saturation. *IEEE Trans. Ind. Appl.* **58** (3), 3637–3651 (2022). May.-Jun.
12. Farhan, A. et al. Aug., Advanced strategy of speed predictive control for nonlinear synchronous reluctance motors. *Machines*, **8**, 3, 44, (2020).
13. Lin, F. J., Chen, S. G., Huang, M. S., Liang, C. H. & Liao, C. H. Adaptive Complementary Sliding Mode Control for Synchronous Reluctance Motor With Direct-Axis Current Control, *IEEE Transactions on Industrial Electronics*, Vol. 69, No. 1, 141–150, Jan. (2022).
14. Chen, L. et al. May., Continuous Adaptive Fast Terminal Sliding Mode-Based Speed Regulation Control of PMSM Drive via Improved Super-Twisting Observer, *IEEE Transactions on Industrial Electronics*, Vol. 71, No. 5, 5105–5115, (2024).
15. Wang, Y., Yan, F., Chen, J. & Chen, B. Continuous Nonsingular Fast Terminal Sliding Mode Control of Cable-Driven Manipulators With Super-Twisting Algorithm, *IEEE Access*, Vol. 6, 49626–49636, Sep. (2018).
16. Li, K., Ding, J., Sun, X. & Tian, X. Overview of Sliding Mode Control Technology for Permanent Magnet Synchronous Motor System, *IEEE Access*, Vol. 12, 71685–71704, May. (2024).
17. Benbouhenni, H. et al. Jan., Enhancing the power quality of dual rotor wind turbines using improved fuzzy space vector modulation and super twisting sliding techniques. *Scientific Reports*, **15**, 1, 7290, (2025).
18. Tan, J., Zhou, Z., Zhu, X. & Xu, X. Fast super twisting algorithm and its application to attitude control of flying wing UAV. *Control Decis.* **31** (1), 143–148 (Jan. 2016).
19. Song, Z. & Zhou, W. PMSM disturbance resistant adaptive fast Super-Twisting algorithm speed control method. *IEEE Access.* **12**, 138155–138165 (2024).
20. Hou, Q. & Ding, S. GPIO Based Super-Twisting Sliding Mode Control for PMSM, *IEEE Transactions on Circuits and Systems II: Express Briefs*, Vol. 68, No. 2, 747–751, Feb. (2021).
21. Ding, S., Hou, Q. & Wang, H. Disturbance-Observer-Based Second-Order Sliding Mode Controller for Speed Control of PMSM Drives, *IEEE Transactions on Energy Conversion*, Vol. 38, No. 1, 100–110, Mar. (2023).
22. Hameed, A. H., Al-Samarraie, S. A. & Humaidi, A. J. One-Instant flux observer design for Three-Phase induction motor with reduced bound active load rejection speed controller. *Anais Da Acad. Brasileira De Ciências*, **96**, No. (2025). suppl 3, e20240539, Jan.
23. Hou, Q., Ding, S. & Yu, X. Composite Super-Twisting Sliding Mode Control Design for PMSM Speed Regulation Problem Based on a Novel Disturbance Observer, *IEEE Transactions on Energy Conversion*, Vol. 36, No. 4, 2591–2599, Dec. (2021).
24. Hu, M., Ahn, H., Chung, Y. & You, K. Speed regulation for PMSM with super-twisting sliding-mode controller via disturbance observer. *Mathematics* **11** (7), 1618 (2023).
25. Chen, Y. & Liu, X. A variable rate Super-twisting sliding mode speed control with overcurrent protection for PMSM considering aperiodic and periodic disturbances. *IEEE Trans. Power Electron.* **40** (4), 5787–5798 (April 2025).
26. Lin, W. B. & Chiang, H. K. Super-Twisting Algorithm Second-Order Sliding Mode Control for a Synchronous Reluctance Motor Speed Drive, *Mathematical Problems in Engineering*, Vol. No. 1, 632061, 2013. (2013).
27. Selma, B., Bounadja, E., Belmadani, B. & Selma, B. Improved performance and robustness of synchronous reluctance machine control using an advanced sliding mode and direct vector control, *Advanced Control for Applications: Engineering and Industrial Systems*, Vol. 6, No. 1, e178, Mar. (2024).
28. Liu, Y. C. Disturbance-Observer-Based Sliding-Mode speed control for synchronous reluctance motor drives via generalized Super-Twisting algorithm. *Actuators*, Vol. 13,7, 233, Jun. 2024.
29. Nasim, U. et al. Finite-time robust speed control of synchronous reluctance motor using disturbance rejection sliding mode control with advanced reaching law. *Plos One*, **18**, 9, e0291042, Sep. (2023).
30. Ren, L. et al. Adaptive nonsingular finite-time terminal sliding mode control for synchronous reluctance motor. *IEEE Access.* **9**, 51283–51293 (2021).
31. Heidari, H. et al. Feb., A review of synchronous reluctance motor-drive advancements. *Sustainability*, **13**, 2, 729, (2021).
32. Li, C., Wang, G., Zhang, G., Xu, D. & Xiao, D. Saliency-Based Sensorless Control for SynRM Drives With Suppression of Position Estimation Error, *IEEE Transactions on Industrial Electronics*, Vol. 66, No. 8, 5839–5849, Aug. (2019).
33. Xu, X. Y., Wang, Y. C. & Shen, J. X. Direct torque control-Space vector modulation control strategy of synchronous reluctance motor based on maximum torque Per-Ampere. *Trans. China Electrotechnical Soc.* **35**(2), 5839–5849 (2020).
34. Choi, J. W. & Lee, S. C. Antiwindup Strategy for PI-Type Speed Controller, *IEEE Transactions on Industrial Electronics*, Vol. 56, No. 6, 2039–2046, Jun. (2009).

Author contributions

Y.N. and Z.H. designed the research, developed the methodology, and performed the modeling, simulation, and experimental work. Z.H. wrote the original manuscript. H.H. and R.L. prepared the equations, figures, and tables. Y.N., W.S., and J.H. reviewed and edited the manuscript.

Funding

This research was supported by corporate funding (HVSLDS5 Series Synchronous Reluctance Motor and Controller Development Project, No. 24B0353).

Declarations

Competing interests

The authors declare no competing interests.

Additional information

Correspondence and requests for materials should be addressed to Y.N.